Morphological and electrochemical characterization of nanostructured $Li_4Ti_5O_{12}$ electrodes using multiple imaging mode synchrotron X-ray computed tomography

Ali Ghorbani Kashkooli[1], Evan Foreman[2], Siamak Farhad[2*], Dong Un Lee[1], Kun Feng[1], Gregory Lui[1], Vincent De Andrade[3], Zhongwei Chen[1*]

[1]Department of Chemical Engineering, Waterloo Institute for Nanotechnology, Waterloo Institute for Sustainable Energy, University of Waterloo, Waterloo, ON N2L 3G1, Canada

[2]Department of Mechanical Engineering, University of Akron, Akron, OH 44325-3903, USA

[3]Advance Photon Source, Argonne National Laboratory, Lemont, IL 60439, USA

Abstract

In this study, synchrotron X-ray computed tomography has been utilized using two different imaging modes, absorption and Zernike phase contrast, to reconstruct the real three-dimensional (3D) morphology of nanostructured $Li_4Ti_5O_{12}$ (LTO) electrodes. The morphology of the high atomic number active material has been obtained using the absorption contrast mode, whereas the percolated solid network composed of active material and carbon-doped polymer binder domain (CBD) has been obtained using the Zernike phase contrast mode. The 3D absorption contrast image revealed that some LTO nano-particles tend to agglomerate and form secondary micro-sized particles with varying degrees of sphericity. The tortuosity of electrode's pore and solid phases were found to have directional dependence, different from Bruggeman's tortuosity commonly used in macro-homogeneous models. The electrode's heterogeneous structure was investigated by developing a numerical model to simulate galvanostatic discharge process using the Zernike phase contrast mode. The inclusion of CBD in the Zernike phase contrast results in an integrated percolated network of active material and CBD that is highly suited for continuum modeling. The simulation results

*Corresponding authors: sfarhad@uwakron.edu; zhwchen@uwaterloo.ca

highlight the importance of using the real 3D geometry since the spatial distribution of physical and electrochemical properties have a strong non-uniformity due to microstructural heterogeneities.

Keywords: Lithium-ion battery, Synchrotron X-ray computed tomography, lithium titanate oxide, Tortuosity, Image based modeling.

1. Introduction

Lithium-ion batteries (LIBs) are currently the leading energy store system technology that fuels consumer electronics and electrified vehicles with high efficiency and performance. The high performance LIB requires high capacity active material and optimized electrode structure [1–3] which directly influence the overall cell performance such as rate capability, cycle life, and safety [4–6]. For example, using in-situ measurement of lithium transport Harris *et al* [6] showed the necessity for microstructural information to study lithium plating and dendrite growth in a graphite anode during the battery charging process.

Recently, application of tomographic techniques including focused ion-beam scanning/electron microscopy (FIB/SEM) [7–9] and X-ray tomography (XCT) [10–12] have provided the microstructural details required for LIB research. The reconstructed microstructures effectively reveal the three-dimensional (3D) morphological information and spatial heterogeneity of porous electrodes. In the case of using nano-XCT, LIB electrodes can be scanned using two different imaging modes: 1) the absorption contrast mode, where the contrast is generated by X-ray absorptivity of the sample, and 2) the Zernike phase contrast mode, where the contrast occurred by phase shift of the X-ray passing through the sample is captured [13]. A realistic 3D reconstruction of LIB porous electrodes must clearly distinguish three domains: active material, carbon-doped polymer binder domain (CBD), and pore domain. The X-ray attenuation is a function of atomic number and density of material. Therefore,

the absorption contrast captures only the highly-attenuated cathode active material, while leaving the remainder of the volume as a combination of pore domain and CBD. The lack of CBD inclusion in the absorption contrast images causes a discontinuity within the electrode solid domain [14], which significantly decreases the accuracy of solid domain transport properties estimation such as tortuosity [15,16]. On the other hand, using the Zernike phase contrast mode, active materials can be imaged along with the CBD [16], which is why it is typically used in imaging of low-attenuation, low atomic number materials commonly used in LIBs such as graphite and polymer binders [13,17]. As X-ray penetrates the sample, both amplitude reduction (active material imaging) and phase change (CBD imaging) of the beam occurs resulting in attenuation and refraction of the X-ray. Therefore, the Zernike phase contrast guarantees a connected electrode solid domain comprising a percolated network of active materials surrounded by CBD which is highly suited for simulation studies.

Most of the studies based on simulations describe LIB electrodes as a macro-homogeneous isotropic porous medium using scalar properties such as particle size, porosity, diffusivity, and conductivity [18–20]. Electrode tortuosity is usually used to describe the decrease in the effective transport properties due to geometric complexities inherent to porous materials. The most common approach to calculate tortuosity is using Bruggeman relation [21]:

$$\tau = \varepsilon^{1-\alpha} \tag{1}$$

which describes tortuosity τ as a function of porosity ε and the Bruggeman exponent. The value of $\alpha = 1.5$ has been widely used in macro-homogeneous models to calculate effective diffusivity and conductivity. The value was originally obtained from the transport study of a porous medium consisting of equally sized sphere pores [7,22]. However, the validity of Bruggeman relation with $\alpha = 1.5$ is controversial. For nano-particle LIB electrodes, Thorat *et al.* used AC impedance and polarization interrupt experimental methods to investigate tortuosity-porosity of $LiFePO_4$ electrodes [23]. They showed that Bruggeman exponent accurately predicted the tortuosity of solid domain, while

predicted the pore domain tortuosity less by a factor of 2. Conversely, using heat/mass transport analogy simulation, Ender et al. showed that $LiFePO_4$ electrode pore domain tortuosity agrees quite well with Bruggeman relation [8], whereas the solid domain tortuosity found to be two times the one predicted by Bruggeman. Cooper *et al.* measured the pore domain tortuosity by heat transport simulation and showed that Bruggeman had underestimated the tortuosity of the $LiFePO_4$ electrode [24]. They showed that tortuosity is highly dependent on the direction and should be considered as a vector rather than a scalar in macro-homogeneous models. We also reconstructed a 3D morphology of $LiFePO_4$ electrode's solid domain using nano-XCT in our previous study to estimate the directional tortuosity [25]. The estimated tortuosities were then employed to simulate the electrochemical performance of the electrode at higher length scales in a multiscale modeling framework. Recently, Shearing group provided a great review on the origin and limitations of Bruggeman relation and compared several studies on the tortuosity-porosity correlation [22]. They concluded that Bruggeman equation provides better results when applied to media with sphere or cylinder particles, while special considerations are needed for more complex geometries.

The battery performance can be sufficiently predicted using effective transport properties based on the tortuosity concept, as in macro-homogeneous models. However, the inclusion of real 3D electrode structures is crucial for electrode degradation since failures depend on local inhomogeneities [26]. XCT has enabled the analysis of electrode's local structural effects on physical and electrochemical property distributions. For instance, transport and electrochemical properties within electrodes are obtained during battery charge/discharge processes. Generally, the distribution of these properties are heterogeneous because the electrode structures are heterogeneous [27,28], however, the link between XCT data and performance effectively allows quantification of these heterogeneities inside the electrodes.

Herein, we present, to the authors' best knowledge, the first 3D microstructural study of $Li_4Ti_5O_{12}$

(LTO) electrode based on multiple imaging mode synchrotron nano-XCT data. LTO is regarded as one of the most promising candidates as an effective LIB anode [29,30]. To overcome its inherently low conductivity and sluggish lithium diffusivity, nano-structuring of LTO has been proven to be a viable approach [18]. However, it poses a marked challenge for microstructural imaging due to the requirement of high resolution (below 100 nm) [24,25]. For this, a synchrotron transmission X-ray microscopy (TXM) with spatial voxel resolution of 58 nm^3 at the Advanced Photon Source (APS) of the Argonne National Laboratory (ANL) has been employed. The data is obtained in both the absorption contrast and Zernike phase contrast modes. While the absorption contrast is used to study the morphological characteristics of primary and secondary active material particles, the Zernike phase contrast is combined with absorption contrast to resolve CBD within the electrodes. Cooper *et al.* imaged nano-particle $LiFePO_4$ cathodes using nano-XCT and explored the microstructural heterogeneity within the 3D reconstructed pore domain based on the tortuosity calculations [24]. Similarly, we have employed the absorption and Zernike phase contrast reconstructed structures as the foundation to determine electrode tortuosities for pore and solid domains, respectively. The geometrical and transport based tortuosities are estimated to shed light on the complex anisotropic nature of heterogeneous electrodes. In addition to tortuosity, the effects of local microstructural heterogeneity on the physical and electrochemical processes that occurs during the cell operation have been investigated. For this, a galvanostatic discharge performance of the half-cell LTO electrode is simulated based on our recently published work on representative volume element (RVE) model developed for LIB [28]. Nano-XCT simulation studies typically use absorption contrast 3D reconstructed as the model geometry [25,31]. As mentioned, CBD cannot be distinguished from the pore domain in this mode, which may lead to isolated active material particles. Image processing techniques are usually employed to merge the active materials together and form an integrated solid domain required for continuum simulations [24,25,31]. However, Zernike phase contrast geometry

employed in the current model provides a united percolated network of active materials and CBD, completely eliminating possible error associated with 3D reconstruction. Our previous RVE model [28] is further improved in this work by incorporating the charge transport within the microstructures to the governing equations. Specifically, the model includes conservation of mass and charge within the solid domain and the intercalation kinetics. The simulated performance is validated with the experimental data obtained from half/coin-cell performance testing. The model does not consider the local variation of lithium-ion concentration inside the electrolyte, instead an electrolyte resistance term is employed to account for the electrolyte resistance.

This paper is organized as follows: first, the electrode fabrication and imaging techniques used to obtain the 3D reconstructed morphology of LIB electrode are described. Then, the Finite Element (FEM) basis for calculating tortuosity using heat/mass transport analogy is reviewed. Then, the modeling development including RVE selection, followed by the governing equations used to simulate electrochemical performance are presented. Finally, the simulation results are demonstrated and discussed with concluding remarks.

2. Experimental

2.1. Material synthesis and Electrode/half-cell fabrication

LTO nano-particle was synthesized using a simple two-step route as follows: 1) synthesis of monodisperse TiO_2 particles; and 2) solid-state conversion of TiO_2 to LTO particles using carbon as a means of blocking Ti diffusion and suppressing TiO_2 sintering [32]. For the details of synthesis procedure and LTO characterizations readers are referred to our previous publication[18]. The electrode slurry was prepared by mixing 90 wt% LTO nano-powder, 5 wt% polyvinylidene fluoride (PVdF) as a binder, and 5 wt% Super P carbon black as conducting agent in 1-methyl-2-pyrrolidinone (NMP). The resultant slurry was then casted on a copper foil current collector using

the doctor blade. The electrodes were punched in 10 mm diameter and dried in a vacuum oven at 100°C for 12 hours.

Four coin half-cells were fabricated to evaluate electrochemical performance of the electrodes. All cells were fabricated in identical conditions to assure the repeatability of results. The coin cells utilized a lithium-foil as the reference/counter electrode, a Celgard 2500 as separator, and a 3:7 *(v/v)* ethylene carbonate and dimethyl carbonate organic solution containing 1.0 M hexafluorophosphate ($LiPF_6$) as the electrolyte. Coin cells were assembled in an argon-filled glove box (H_2O < 0.5 ppm, O_2 < 0.5 ppm). Charge-discharge cycling was conducted using a NEWARE BTS-5V 10mA battery testing station. All cells were cycled at C rates ranging from 0.2 C to 5 C (theoretical capacity of LTO, C = 175 mAh/g) within a voltage window of 1.0-2.5 V.

2.2. Nano-XCT

The electrode's sample for X-ray imaging was obtained by dissolving electrode's copper foil in nitric acid. Since copper influences the X-ray attenuation, the current collector needed to be delaminated. Synchrotron radiation nano-XCT was conducted using Transmission X-ray Microscope at Advanced Photon Source (APS), Argonne National Laboratory (sector 32-ID-C) [33]. Tomographic data was obtained using an 8 keV monochromatic beam. The tomographic images were obtained by rotating the sample 180° using a step scan increment of 0.5° and the exposure time of 1 second at each increment. The X-ray objective lens used to magnify radiographs was a 58 nm outermost zone width Fresnel zone plate, providing a spatial resolution of 58 nm. The 3D reconstruction was performed with Tomopy, an open source collaborative framework for the analysis of synchrotron tomographic data [34,35]. The reconstructed volume represents voxel of attenuation coefficient with a width of 58 nm after binning. The total number of virtual slices were 1024 with 58 nm cubic voxels resolution and field of view of 1024 × 1224 × 1224 voxels. The LTO sample was imaged using two imaging modes: absorption contrast and Zernike phase contrast.

Image processing and segmentation of grayscale 3D image was achieved using a commercial software Simpleware ScanIP (Synopsys, Mountain View, USA). First, to reduce background image noise, a median filter with the cubic neighborhood radius of 3 pixels was applied. Median filter is effective to remove salt-and-pepper noise and remove the outliers. It computes the value of each pixel as the statistical median of the neighborhood pixel around the corresponding pixel. Then, a mean filter with the cubic neighborhood radius of 1 pixel was applied for further noise reduction. The filter finds the value of each pixel by calculating the statistical mean of the neighboring pixels. Segmentation is achieved using binary thresholding. Unwanted noise and details was removed using recursive Gaussian filter with cubic Gaussian sigma value of 1. Gaussian sigma is a parameter that determines how many neighboring pixels should contribute to the smoothing operation of corresponding pixel. The larger the sigma, the stronger the smoothing. To form 3D pore network, a copy of the pore domain is created and then inverted on all slices in the whole cubic domain. This is similar to the Boolean operation usually employed elsewhere, where the solid domain is subtracted from the cubic solid.

Figure 1a and 1b show two raw virtual slices obtained from absorption contrast and Zernike phase contrast modes, respectively. With relatively larger field of view of ~70 µm, and having primary nano-particles size < 200 nm, it is hard to differentiate various components such as active material and CBD in the virtual slices. Therefore, we zoomed on a smaller cubic region with the side of 10.4 μm^3, to distinguish between absorption and Zernike phase contrast images. Fig. 1c and 1d show cubic grayscale image of the electrode from reconstructed morphology based on absorption contrast and Zernike phase contrast, respectively (the cube side is 10.4 µm corresponding to 180 × 180 × 180 voxels). In absorption contrast, white region represents the active material and black region shows the pores plus CBD (see Fig. 1c), whereas in Zernike phase contrast, white region represents active material plus CBD and black region shows the pores (see Fig. 1d). Fig. 1e and 1f show binary

segmented regions obtained from the absorption contrast and Zernike phase contrast modes, respectively, which are applied to the image processing steps described. As previously shown by Babu *et al* [16] the active material and CBD could be separately resolved by combining absorption contrast and Zernike phase contrast images. As mentioned, in absorption contrast, solid domain comprises active material, whereas in Zernike phase contrast, it includes active material as well as CBD. To capture the CBD, absorption contrast image needs to be subtracted from Zernike phase contrast to eliminate the active material. Fig. 1g shows the segmented 2D tomogram of the LTO electrode. In this figure, the domains of the active material, CBD, and pore separated from each other can be easily distinguished. A 3D image of the electrode's solid domain distinguishing active material and CBD is demonstrated in Fig. 1h. In addition, Table 1 compares the volume fraction of different electrode phases obtained from XCT reconstruction and electrode fabrication. The electrode fabrication fraction were calculated based on the actual mass ratio (90:5:5) and material density ($\rho_{LTO} = 3.5\ g/cm^3, \rho_{CB} = 1.8\ g/cm^3, \rho_{PVDF} = 1.77\ g/cm^3$). The small deviation in volume fractions is attributed to XCT low resolutions wherein the structure sizes below 58 nm^3 could not be captured.

Table 1. The volume fraction of different phases of the nanostructured LTO electrode based on the reconstruction data and the actual mass ratio.

	XCT	Electrode fabrication
LTO	0.33 (absorption contrast)	0.35
LTO+CBD	0.43 (Zernike phase contrast)	0.43
CBD	0.10	0.08
Pore	0.57	0.57

The lack of CBD in absorption contrast images may cause isolated LTO particles. This can increase computational costs due to having multiple regions in solid domains. In literature, a filter or a dilation function on the solid domain is commonly employed to preserve the domain connectivity [14], [25] or alternatively, very low content of carbon black (3%) and binder (3%) are added to the electrode during fabrication to reduce the reconstruction error [36]. However, the Zernike phase contrast reconstructed structure used in this study, provides a united percolated network of active materials and CBD, suitable for the FEM simulation (see Fig. 1g). This eliminates the error associated with neglecting low density carbon and binder phase in synchrotron based FEM simulations.

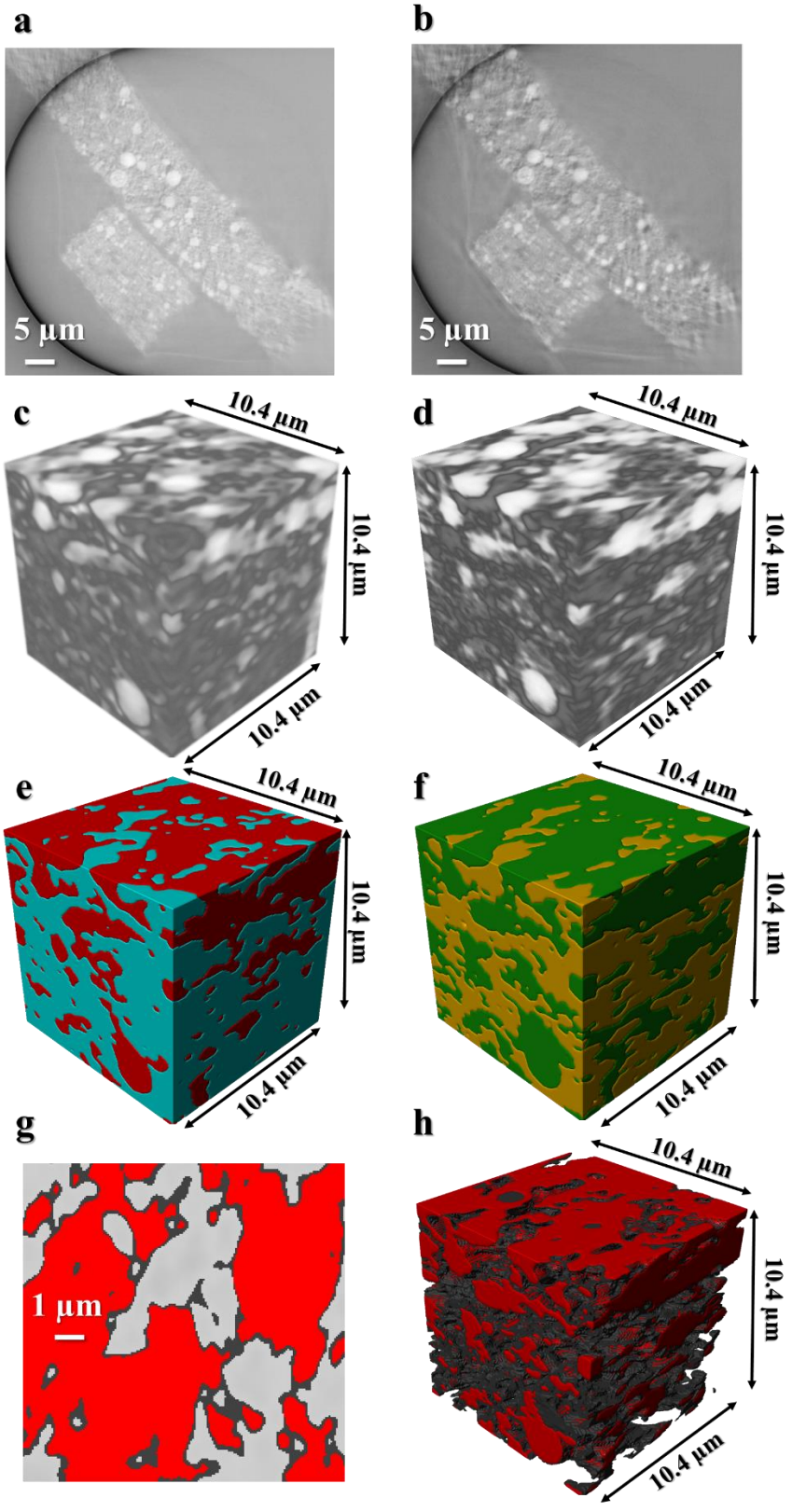

Figure 1. Raw grayscale 2D morphology of the electrode obtained using a) absorption contrast, and b) Zernike phase contrast imaging modes. Reconstructed 3D microstructure c)

absorption contrast and d) Zernike phase contrast. Segmentation of the regions using e) absorption contrast (red: active material, light blue: pores plus CBD) and f) Zernike phase contrast (green: active material plus CBD, dark yellow: pores). Active material (red), CBD (dark gray) and electrolyte (light gray) are distinguished by combining absorption and Zernike phase contrast imaging modes: g) 2D tomogram and h) 3D reconstruction.

3. Modeling

3.1. Morphological and transport properties

Various morphological characteristics are purely geometrical and do not require numerical simulation. We quantified morphological parameters including electrode porosity, ε, volume specific surface area, a, and geometrical tortuosity, τ_{geom}, as morphological characteristics. The electrode porosity, ε, and volume specific surface area, a, are critical inputs for macro-homogeneous models. In case of volume specific surface area, macro-homogeneous models usually use simplified geometry such as: single-sized and multi-sized spherical particles, or complex computer generated geometries. The volume specific surface area is then estimated based on the assumed structure. For example, for spherical particles, the volume specific surface area of the electrode, can be computed using the relationship [19,37]:

$$a = \frac{3\,(1-\varepsilon)}{R_s} \tag{2}$$

where, R_s, is the average particle size.

The original 3D reconstruction of the electrode sample was a non-cubic geometry that was later cropped to the largest possible cubic volume with the size of 260 × 800 × 800 voxels corresponding to the overall volume of 29216 μm^3. For the estimation of transport properties, a region with 180 × 180 × 590 corresponding to 3730 μm^3 was chosen (See Fig. 2 for the pore domain demonstration of the region). Although the selected region includes just 11% of the original image volume, this region is quite large compared to the nano-size of active material particles. There are two types of tortuosity:

1) geometrical tortuosity, which is the ratio of the actual path length between two points to their Euclidean distance (straight line distance); 2) transport tortuosity, which accounts for the decrease of transport phenomena due to the geometrical complexity of pores network. Geometrical tortuosity is calculated by dividing the actual path length between two points by the straight-line distance. The average geometrical tortuosity in each direction is estimated using the relationship [8]:

$$\tau_{geom} = \langle \frac{\min(L)}{D} \rangle \tag{3}$$

where τ_{geom}, is the average of the shortest centroid path length, L, through the microstructure divided by D, which is the straight-line distance. To obtain transport tortuosity, a FEM simulation on the pore and solid domains are performed, where the diffusion and conduction are described by Laplace equation:

$$\nabla.(k\nabla T) = 0 \tag{4}$$

In this equation, k is the transport coefficient (i.e. diffusivity or thermal conductivity or electrical conductivity) and T is the Temperature. Fig. 2 shows the reconstructed pore domain, based on absorption contrast, used for the transport tortuosity estimation. For each directional tortuosity, temperature is arbitrarily set as 0 and 1 at inlet and outlet faces of cubic domain, respectively, and the heat flux is specified as zero at all other boundaries. From the simulation results, J, the area heat flux integral at the outlet or inlet boundary is calculated by:

$$J = \int_S k \frac{\partial T}{\partial x_i} dS \tag{5}$$

where, S is the outlet or inlet surface boundary, and i is the coordinate direction. Then, the effective conductivity, k_{eff}, is calculated using the equation,

$$k_{eff} = \frac{J}{A}\frac{L}{\Delta T} \tag{6}$$

where, ΔT is the temperature difference two opposite walls, which was set to 1, A is the cross section area perpendicular to the heat transfer direction, and L is the distance between inlet and outlet boundary. Tortuosity is given by the equation:

$$\tau = \frac{\varepsilon\, k}{k_{eff}} \tag{7}$$

If we place Eq. (5) and (6) into Eq. (7), transport tortuosity can be calculated by:

$$\tau_i = \frac{\varepsilon\, A}{L \int_S \frac{\partial T}{\partial x_i} dS} \tag{8}$$

Eq. (8) shows that transport tortuosity, τ_i, is not a function of thermal conductivity, k, and the tortuosity factor is the same for all transport phenomena including heat and mass transport. The same approach can be applied on the reconstructed solid domain which is not shown here for the similarity.

As previously mentioned, 1D micro-homogenous models commonly use Bruggeman correlation (see Eq. (1)) with $\alpha = 1.5$ as the basis for calculating tortuosity. Bruggeman equation is based on the transport study with the assumption of isotropic and homogeneous pore domain. This assumption provides one unique tortuosity for the whole electrode. To be able to compare the directional tortuosities obtained from 3D simulation to Bruggeman torsuosity, Cooper *et al* [24] introduced a characteristic tortuosity τ_c as:

$$\tau_c = 3\left[{\tau_x}^{-1} + {\tau_y}^{-1} + {\tau_z}^{-1}\right]^{-1} \tag{9}$$

where, τ_x, τ_y, τ_z are directional tortousities. The authors also suggested that this quantity can be used in the 1D micro-homogeneous model.

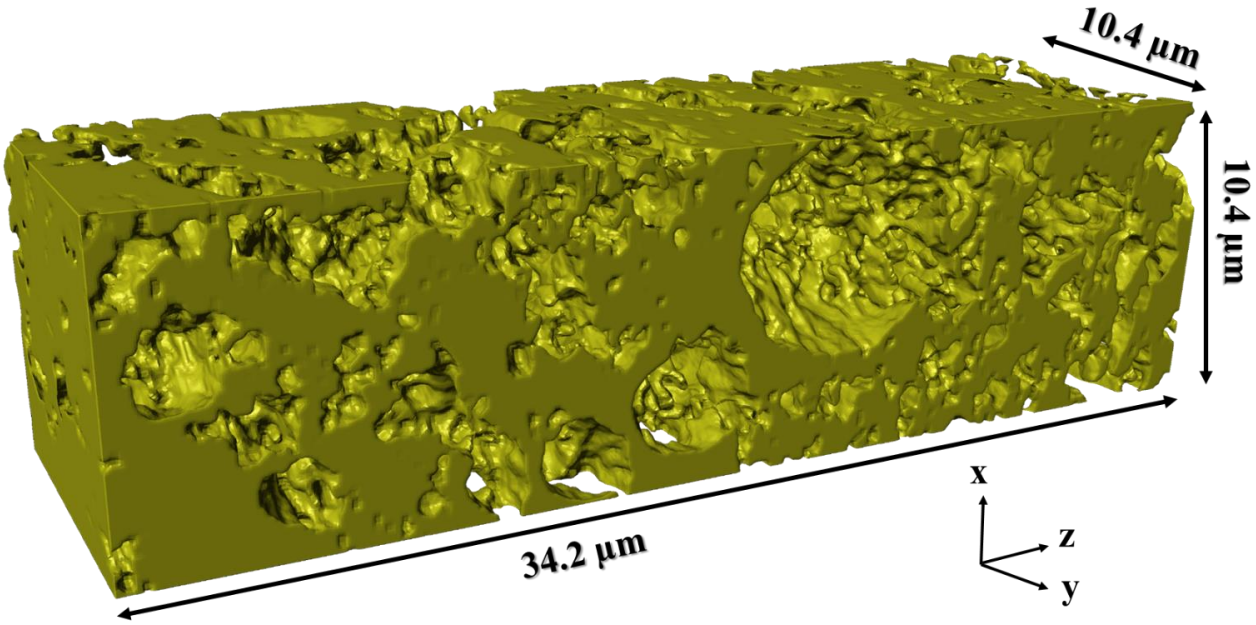

Figure 2. 3D visualization of the LTO electrode's pore domain obtained using nano-XCT in absorption contrast mode. The structure size is 10.4 × 10.4 × 34.2 µm^3, which corresponds to 180 × 180 × 590 voxels, (The direction of Z is through-plane).

3.2 Electrochemical performance

3.2.1. RVE selection

The electrode RVE is a sub-section volume wherein a measured property can be considered as a representative value for the whole electrode [28]. In this study, the properties of interest for the determination of a suitable RVE size are the electrode's porosity and volume specific surface area that is the ratio of interfacial solid/pore domains surface area to the electrode volume. Table 2 shows sample volume specific surface area and porosity of a cubic RVE sub-section of different sizes obtained from Zernike phase contrast reconstruction. The whole domain porosity is 0.57. For a RVE size of 3.48 µm and larger, the porosity of the sub-sections lies within 2 % of the whole electrode porosity. In addition, the electrode's volume specific surface area is 1.24 (1/µm), thus remaining within 3 % of the domain volume specific surface area for sizes of 3.48 µm and larger. Accordingly,

the smallest appropriate RVE of the electrode is selected as 3.48 μm. This calculation is based on the selection of sub-sections from one corner of electrode sample. To decrease the error associated with the selection of specific region in the electrode position, in the present study, a volume with side length of 7 μm (see Fig. 3) has been selected as the electrode RVE and model geometry for electrochemical performance simulation even though we may have selected the smallest possible size (i.e. 3.48 μm).

Table 2. The electrode's porosity and the solid domain volume specific surface area shown in sub-sections of the electrode sample with various sizes.

Cube size (μm)	Porosity, ε	Volume specific surface area, a ($1/\mu$m)
1.16	0.45	1.40
1.74	0.47	1.37
2.32	0.50	1.39
3.48	0.58	1.26
4.64	0.57	1.22
5.80	0.55	1.26
6.96	0.56	1.29
8.12	0.57	1.26
9.28	0.55	1.22
10.3	0.56	1.24

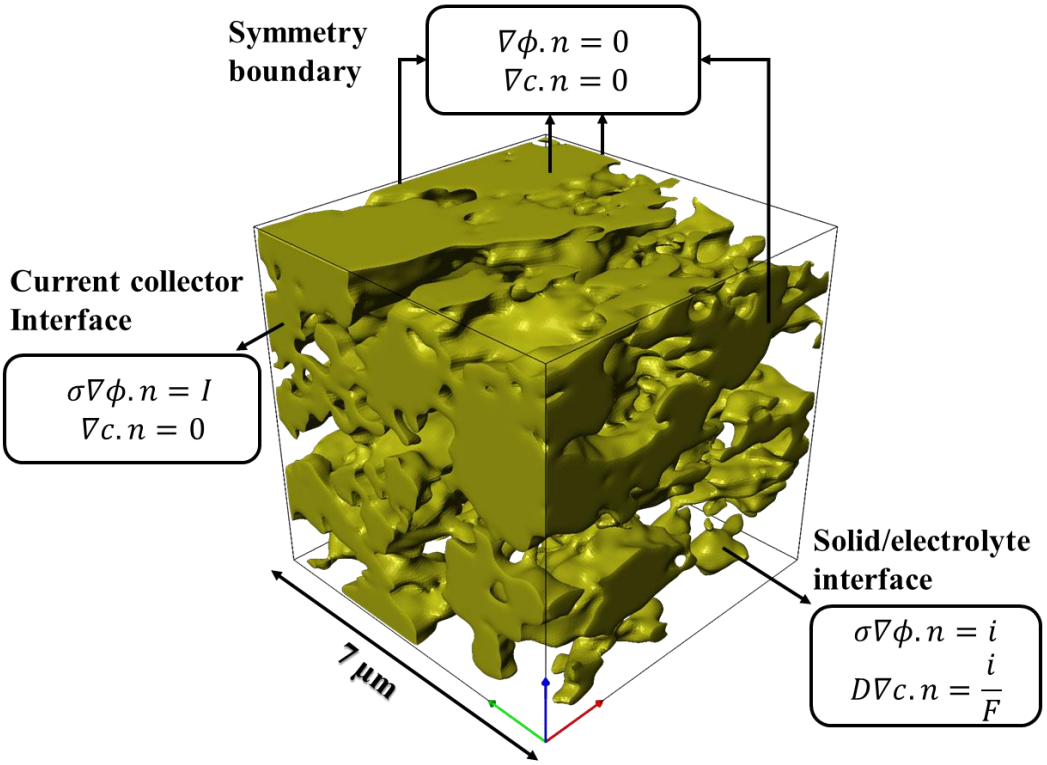

Figure 3. An RVE (cube side length = 7 µm) of the electrode's solid domain extracted from Zernike phase contrast 3D reconstruction for half-cell performance simulation with boundary conditions for specific RVE surfaces used to calculate the governing equations.

3.2.2. Governing equations

The governing equations employed in this study are the conservation of mass and charge within the electrode solid domain. The variations of lithium-ion concentration and electric potential within the electrolyte are neglected and electrolyte polarization has been modeled by a constant resistant parameter. The lithium diffusion within the solid domain is modeled by Fick's mass transport law as [25,31]:

$$\frac{\partial c_1}{\partial t} = \nabla.(D_1 \nabla c_1) \tag{10}$$

where, c_1 is lithium concentration in the RVE, D_1 is the lithium diffusivity in the solid domain, and ∇ operates on the spatial coordinates. To distinguish different regions in the porous electrode, subscripts 1 and 2 are utilized to identify the solid and electrolyte domains, respectively. The electric

potential within solid domain is calculated using ohm's law as:

$$\nabla.(\sigma_1 \nabla \phi_1) = 0 \tag{11}$$

where, ϕ_1 is the electric potential within REV, σ_1 is the solid phase electrical conductivity. As shown in Fig. 3, at the solid/electrolyte interface the boundary conditions for governing equation are [25,31]:

$$D_1 \nabla c_{1,s}.n = j_n \tag{12}$$

$$\sigma_1 \nabla c_{1,s}.n = i_{loc} \tag{13}$$

where, j_n is the normal component of lithium mass transport flux at the solid/electrolyte interface, *s* refers to the solid/electrolyte boundary, and *n* is the normal unit vector to the interface, pointing toward the electrolyte. j_n is depended on applied current density as [28]:

$$j_n = \frac{i_{loc}}{F} = \frac{I}{F(1-\varepsilon)a\mathrm{L}} \tag{14}$$

where, i_{loc} is local current density at the interface, I is the applied current density on the electrode in half-cell, F is Faraday's constant, ε is the electrode porosity, a is the specific surface area of the interface per volume of the solid domain, and L is the electrode thickness. Rate of electrochemical reaction is obtained using Butler-Volmer kinetics as [37]:

$$i_{loc} = i_0 \left(exp\left(\frac{\alpha F}{RT}(\phi_1 - U)\right) - exp\left(-\frac{(1-\alpha)F}{RT}(\phi_1 - U)\right)\right) \tag{15}$$

where, α is charge transfer coefficient, R is the universal gas constant, T is temperature, and U is the open circuit potential and i_0 is the exchange current density defined as [37]:

$$i_0 = F k_0 (c_2)^{\alpha} \left(c_{max} - c_{1,s}\right)^{\alpha} (c_{1,s})^{\alpha} \tag{16}$$

where, k_0 is rate constant of the reaction, c_2 is concentration of lithium-ion in electrolyte which is

considered as a constant in this study.

At the interface of cathode and current collector, j_n needs to be vanished and charge transfer flux should be determined by applied current, I. A symmetric boundary condition is applied on all other surfaces. At the lithium counter electrode, $V = 0$ and separator resistance is neglected. Therefore, the overall half-cell voltage can be determined by:

$$E = \phi_1 - IR_2 - U \tag{17}$$

where, R_2 is the electrolyte resistant that represents the potential drop inside the electrolyte between the electrode and lithium foil counter electrode. In this study, R_2 is considered an adjustable parameter that is determined by comparing simulation results with half-cell performance data [38,39].

4. Results and discussion

The SEM image of the LTO electrode consisting of primary nano-particles of size < 200 nm is shown in Fig. 4a. As a comparison, a raw 2D radiograph of the electrode has been obtained from nano-XCT as shown in Fig. 4b, which shows a similar 2D morphology. In addition, because the absorption contrast mode does not capture carbon additives and polymer binder, only the distribution and morphology of the active material particles are observed. The 2D electrode image also demonstrate that some nano-particles are observed to agglomerate and form micron-sized secondary particles (See Fig. 4) that vary in size ranging from 2 to 5 μm. It is noted that due to relatively lower resolution of nano-XCT than SEM, the primary particles inside the secondary particles are not "visible" in nano-XCT images as can be observed in Fig. 4b.

In order to analyze the geometrical morphology of the secondary particles, four well-resolved secondary particles have been selected as shown Fig. 5 with non-uniform surfaces and different morphologies. Table 3 lists the 3D morphological information including size, volume specific

surface area, and sphericity of the four particles. The particle sphericity is determined by dividing the surface area of the particle by the surface area of a sphere with the same volume, with the lower sphericity values indicating stronger non-sphericity. All particles are non-spherical with particle 4 showing the highest degree of non-sphericity, ca. 0.71. Moreover, particles 3 and 4 have sharp sandglass type structures at the corners, which challenges the assumptions made for microstructure homogeneities in conventional macro-homogeneous models. The volume specific surface area of the secondary particles, ~3 (1/μm), is much higher than the one obtained using the Zernike phase contrast mode, 1.24 (1/μm), see Table 2. This could be attributed to the inclusion of CBD in the Zernike phase contrast mode which covers some parts of the particle surface to form electron conduction.

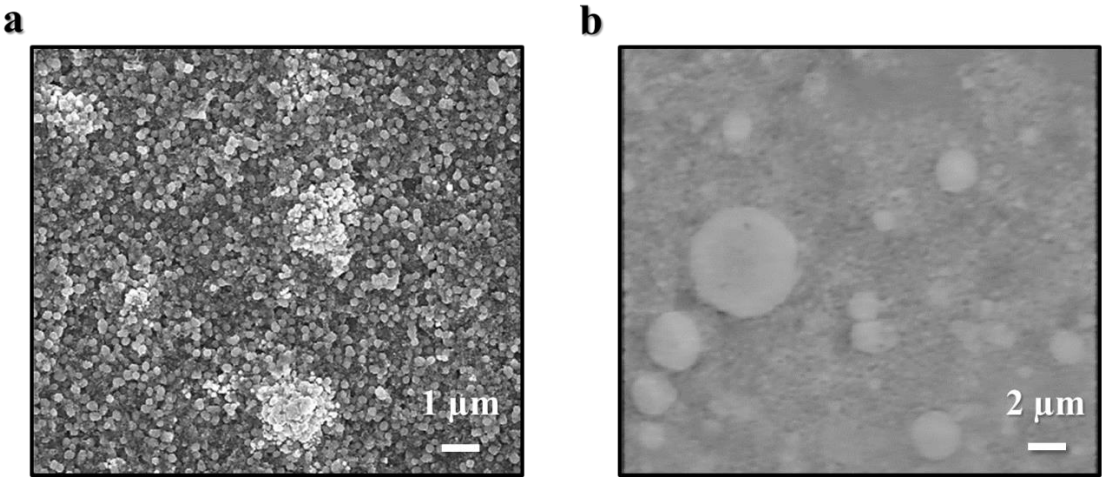

Figure 4. (a) Typical SEM image of LTO electrode, and (b) its 2D radiograph obtained from nano-XCT using the absorption contrast mode.

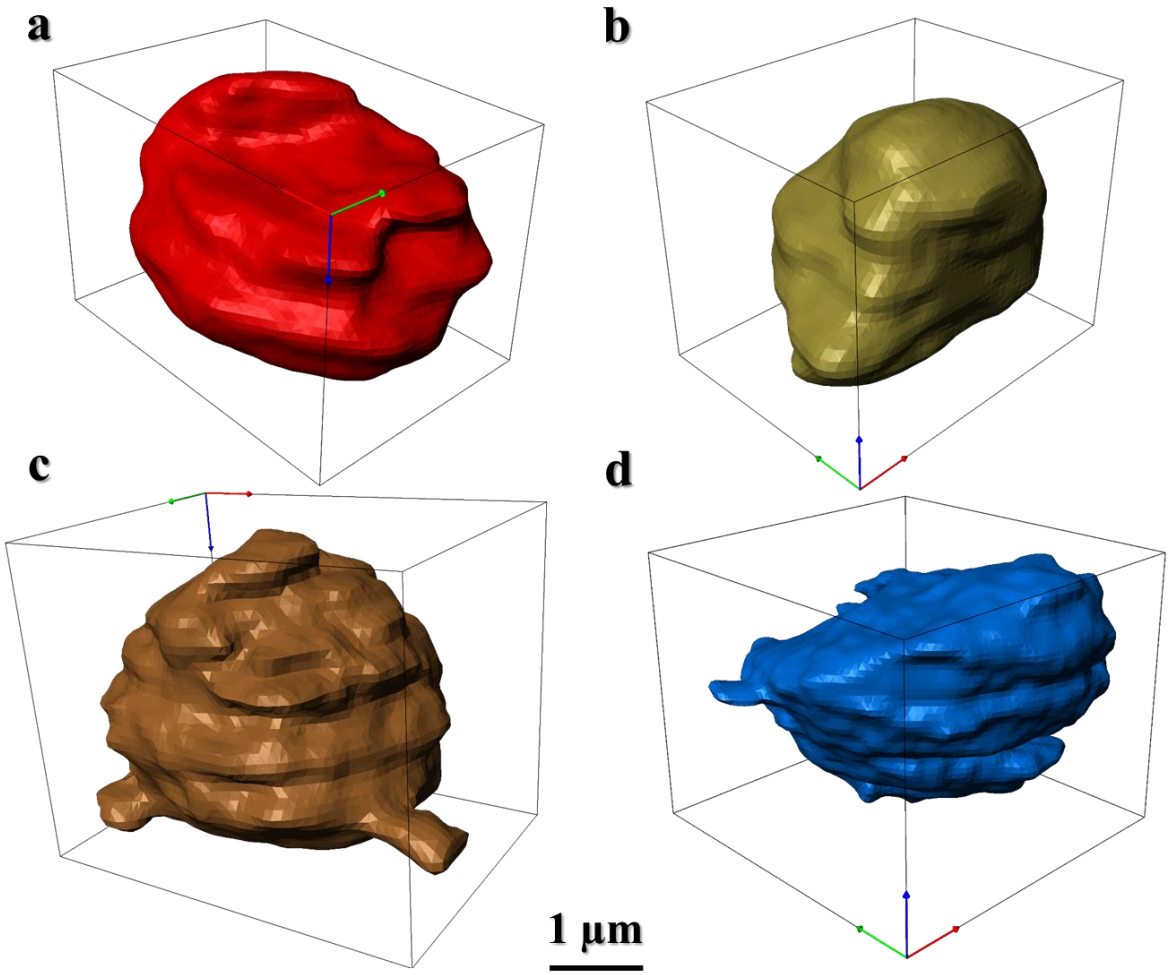

Figure 5. Four isolated LTO secondary particles obtained using the absorption contrast imaging mode. (a) particle (1), (b) particle (2), (c) particle (3), (d) particle (4). The microstructure data for these particles are listed in Table 3.

Table 3. Microstructural information of the four secondary particles obtained using the absorption contrast mode of nano-XCT.

Particle	Sphericity (perfect sphere=1)	Volume specific surface area, a (μm^{-1})	Cube outline dimensions (µm)
1	0.85	3.14	2.96 × 2.08 × 1.96
2	0.93	3.30	2.52 × 1.96 × 1.96
3	0.79	3.62	2.84 × 2.08 × 2.24
4	0.71	3.23	3.36 × 3.48 × 2.68

To investigate the validity of the homogeneity and isotropy of the electrode's microstructure hypothesized in most macro-homogeneous models, transport tortuosities of the pore and solid domains have been simulated and compared in different directions. In case of pore phase geometry, both absorption contrast and Zernike phase contrast modes can be used to reconstruct the model geometry. As mentioned before, the absorption contrast mode includes the volume of CBD in the pore phase. Therefore, the resulting tortuosity obtained using the absorption contrast mode underestimates the pore tortuosity. On the other hand, Zernike phase contrast is not capable of resolving nano-pores within CBD as their size is relatively smaller compared to the resolution of nano-XCT resolution (58 nm). Instead, the CBD is included in the solid domain, which results in enhanced pore phase tortuosity values [7]. In this study, absorption contrast is chosen as the model geometry to quantify pore phase transport tortuosity in agreement with ref. [24]. Alternatively, for solid phase tortuosity, Zernike phase contrast 3D reconstructed structure is employed to provide an inter-connected network for solid structure. This guarantees successful electrons transport within the solid domain.

Table 4 presents the transport tortuosities obtained from heat/mass transport analogy for the solid and pore domains, respectively. In addition, Table 4 shows characteristic tortuosity, τ_c, estimated from the directional tortuosities using Eq. (8) and Bruggeman tortuosity, τ_B, calculated from Eq. (1). Table 4 shows that through-plane tortuosity τ_z, for both pore and solid domains is higher than in-plane τ_x, τ_y, demonstrating higher ionic and electronic transport resistance in the through plane direction. In addition, different directional tortuosity values confirm the inherent heterogeneous structure of electrode, neglected in macro-homogeneous models. Characteristic tortuosity, τ_c for the pore and solid domains are 1.70 and 2.08, respectively, which is higher than the ones predicted by Bruggeman, 1.32 and 1.52. The results show that Bruggeman correlation is a poor estimator of electrode tortuosity. This is due to the fact that Bruggeman is based on homogeneous electrodes with

spherical particles.

Table 4. Porosity and heat transport analogy derived directional tortuosities of the pore and solid phases obtained using absorption contrast and Zernike phase contrast modes, respectively.

	Pore phase	Solid phase
In-plane directional tortuosity, τ_x	1.46	1.37
In-plane directional tortuosity, τ_y	1.69	2.19
Through-plane directional tortuosity, τ_z	2.07	3.86
Characteristics tortuosity, τ_c	1.70	2.08
Bruggeman tortuosity, τ_B	1.32	1.52

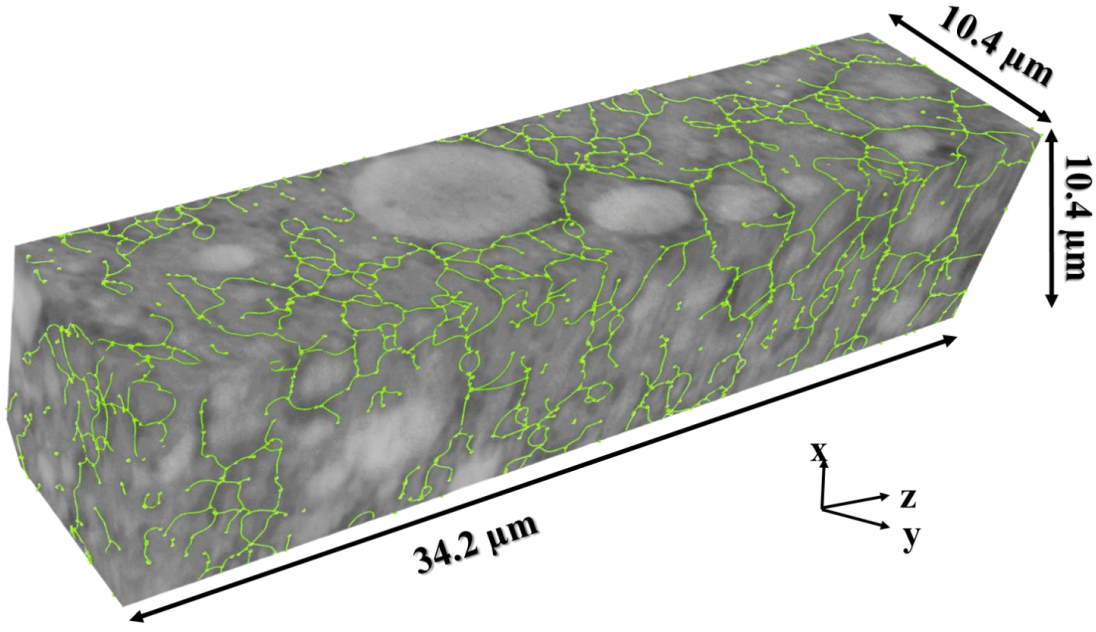

Figure 6. Pore network centroid at the boundaries of the 3D reconstructed electrode. The segmentation is obtained using absorption contrast mode, and the structure size is 10.4 × 10.4 × 34.2 µm^3 which corresponds to 180 × 180 × 590 voxels, (The direction of Z is through-plane).

ScanIP has a function to calculate geometrical tortuosity based on the pore network tortuous paths. In order to calculate geometrical tortuosity, pore network centroid within 3D reconstructed geometry has been constructed as shown in Fig. 6. The tortuosity is then calculated by dividing the centroid motion path between two points length by the straight-line distance. We have estimated the average geometrical tortuosity in each direction according to Eq. (3). Employing Eq. (3) τ_{geom} is averaged over 20 different paths for each starting point on the structure boundary where the end point is located on the opposite boundary. The same approach was used on the solid domain obtained from phase contrast mode. Table 5 demonstrates geometrical tortuosity in each direction along with characteristics tortuosity, τ_c, for both pore and solid domains. The calculated geometrical tortuosities are lower compared to transport based tortuosities, except for τ_x. Moreover, similar to transport tortuosities, geometrical tortuosities also show a clear dependence on direction with higher through-plane tortuosity τ_z, compared to the in-plane τ_x, τ_y. This again confirms the heterogeneous and anisotropic nature of LIB porous electrodes. For $LiFePO_4$ cathode, Cooper *et al.* described a logarithmic relation between geometrical and transport tortuosities for a nano-structured $LiFePO_4$ cathode using various electrode sub-volumes [24]. However, this correlation was not observed in the present study.

Table 5. Surface area and geometrical based directional tortuosities of the pore and solid phases obtained using absorption contrast and Zernike phase contrast modes, respectively.

	Pore phase	Solid phase
In-plane directional tortuosity, τ_x	1.53	1.51
In-plane directional tortuosity, τ_y	1.68	1.94
Through-plane directional tortuosity, τ_z	1.81	2.02
Characteristics tortuosity, τ_c	1.67	1.79

In addition to tortuosity, the electrode microstructures influence the physical and electrochemical properties distribution inside the electrode. Macro-homogeneous models are computationally efficient to predict the LIB performance [18,40,41], however, they employ isotroptic, homogeneous spherical particles in microstructure scale, resulting in a homogeneous distribution of physical and electrochemical properties inside the electrode particles [18]. At the electrode level, they consider the local average value of properties along the direction of electrode thickness, disregarding the microstructural effects[42]. Therefore, property distributions vary along the direction of electrode thickness, and they typically represent a certain trend[42]. On the other hand, heterogeneous models include heterogeneous microstructure of the electrodes as the geometry. This leads to the heterogeneous physical and electrochemical processes which cause the resulting distribution of properties to show no specific trend[31].

Moreover, it is shown that heterogeneities inside the electrode structure contributes to microstructure failure and electrode degradation, which macro-homogeneous models fail to capture. For instance, Wu *et al.* simulated the diffusion induced stress in a 3D reconstructed structure of $LiNi_{0.33}Mn_{0.33}Co_{0.33}O_2$ electrode[14]. They showed that the stress is much higher around the concave regions within the electrode's microstructure than that of smooth homogenous regions due to high local lithium concentrations. Since the stress is higher close to these heterogeneous regions, the mechanical failure could initiate at these areas. Similar results were obtained for $LiCoO_2$ and graphite particles by Lim *et al.*[43] and $LiMn_2O_4$ electrode by Kashkooli *et al.*[44], showing higher stresses around concave heterogeneous regions. Modeling approach based on 3D reconstructed structure, considers the inherent heterogeneous structure of the electrode which makes it an invaluable tool for degradation studies to visualize the real spatial distribution of properties.

To capture the real spatial distribution of these properties, galvanostatic discharge performance of LTO half-cell is simulated using the model presented in Section 3.2. The model geometry used is

the RVE as shown in Fig. 3, which is extracted from the 3D Zernike phase contrast reconstruction. The model parameters, operational conditions, and material properties are listed in Table 6. Fig. 7 shows the galvanostatic discharge performance simulated at different c-rates (solid line). The experimental data obtained from the coin half-cell galvanostatically discharged at various c-rates are also shown in Fig. 7 (dotted line). Model-experimental comparison confirms the model's ability to predict discharge performance of the cell at various rates. The model adjustable parameters including diffusion coefficient, D_{LTO}, reaction rate constant, k_0, electrical conductivity of solid matrix, σ, and electrolyte resistance, R_2, are determined by fitting the model results to experimental data at a low-rate [28,45]. The discharge performance at c-rate=0.2 was chosen as the basis to evaluate adjustable parameters. The values of 1×10^{-15} m^2/s, 1×10^{-10} mol m^{-2}s^{-1}(mol m^{-3})$^{-1.5}$, 0.2 S/m, $2.5 \times 10^{-3}\Omega$m^2 for $D_{LTO}, k_0, \sigma, R_2$ provided the best model-experiment fit and were utilized for the c-rates > 0.1 up to 5 to predict the discharge performance. The open circuit potential, U, of the half-cell was obtained by discharging a fully charged half-cell at very low rate (C/50).

Table 6. The list of model parameters.

Parameter	Description	Value
A	Area of the electrode	0.9698 cm^2
L	Electrode thickness	50 μm
ε	Electrode porosity	0.57
D_{LTO}	Solid state diffusion coefficient of LTO	1×10^{-15} m^2/s
σ	Electrical conductivity of solid matrix	0.2 S/m
k_0	Reaction rate constant	1×10^{-10} mol m^{-2}s^{-1}(mol m^{-3})$^{-1.5}$
α_a	Anodic transfer coefficient	0.5 [46]
α_c	Cathodic transfer coefficient	0.5 [46]
i_f	Exchange current density of lithium foil	19 A/m^2 [46]
c_{ini}	Initial $LiPF_6$ concentration inside electrolyte	1000 mol/m^3

c_{max}	Maximum Lithium concentration in the LTO particles	22741 mol/m^3 [41]
t_+^0	Lithium-ion transference number	0.363 [46]
R_2	Electrolyte resistance	$2.5 \times 10^{-3} \Omega m^2$
T	Cell Temperature	298 K

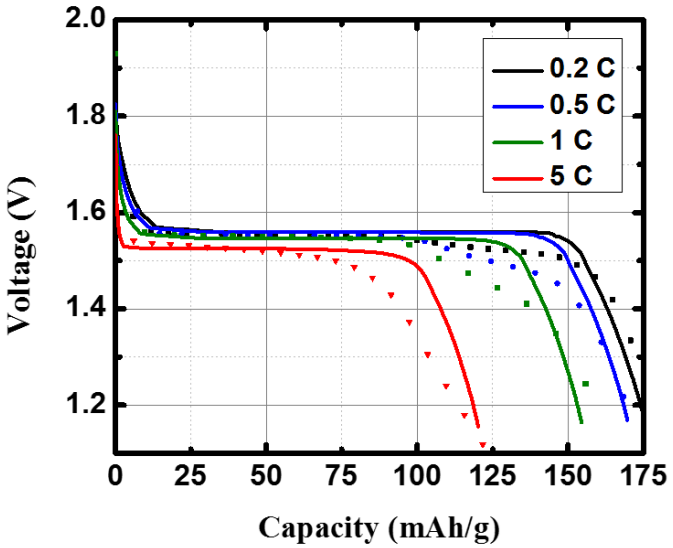

Figure 7. Comparison of the modeling (lines) and experimental coin half-cell (dots) results obtained with the LTO electrode at various C rates.

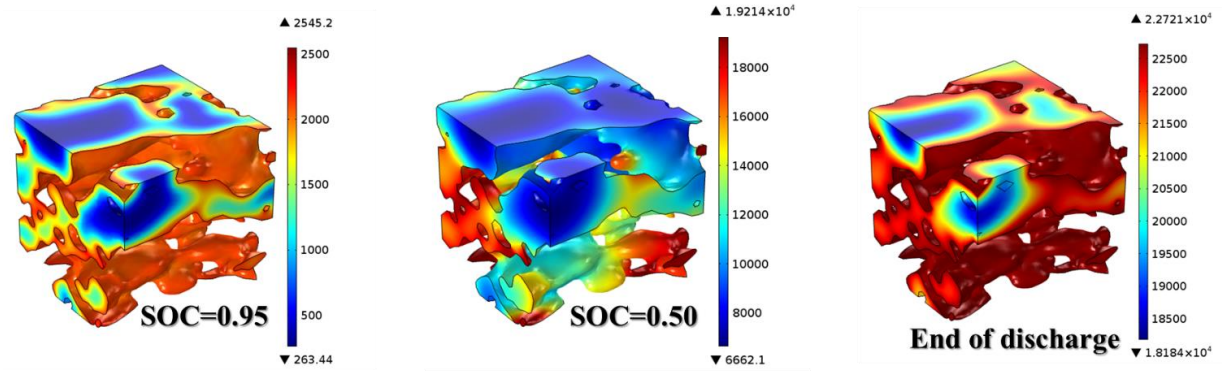

(a) Lithium concentration (mol / m^3)

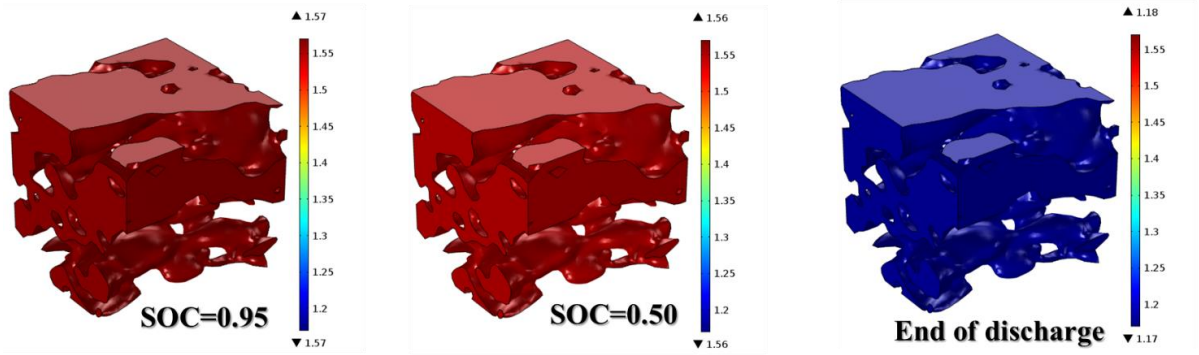

(b) Voltage (V)

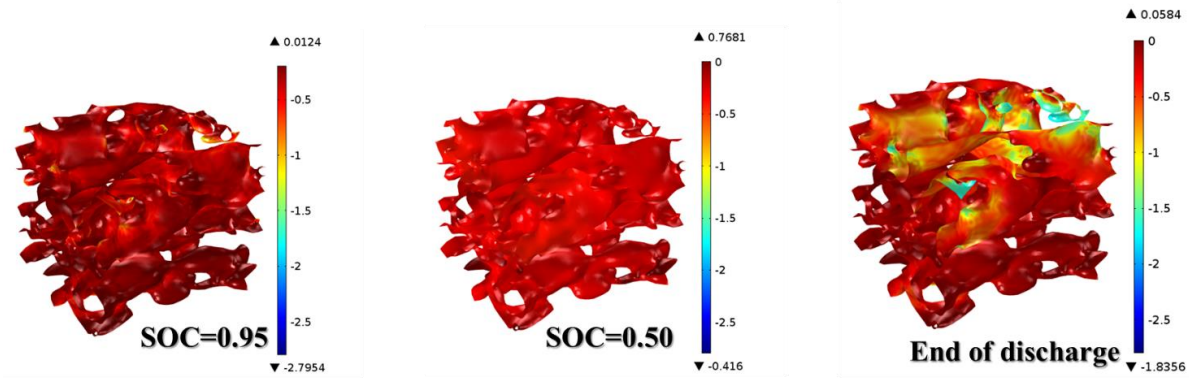

(c) Interfacial current density (A / m^2)

Figure 8. Distribution of physical and electrochemical properties in the RVE shown in Fig. 3 at various states of charge during galvanastatic discharge at 1 C.

The physical and electrochemical property distributions in the electrode's solid domain at different state of charges (SOCs) during the galvanostatic discharge at 1 C are shown in Fig. 8. The SOC is defined as the ratio of remaining discharge time to the time when the end of discharge

happens. The end of discharge is reached when the half-cell voltage drops to 1V. In the present model, lithium can diffuse inside the RVE at the solid/electrolyte interface and assumed free to diffuse between the neighboring particles. Fig. 8a shows that the lithium concentration of smaller particles/microstructures is higher due to higher surface area available for lithium transport specifically in the sandglass type structure with smaller cross section area perpendicular to lithium transport paths. Similar behavior in previous heterogeneous electrode studies were reported [25,28,31]. Fig. 8b shows the voltage variation in the LTO solid phase is very small confirming that nano-structuring and carbon black Super P addition provided the high electronic conductivity. The voltage increases from current collector to the symmetry boundary no more than 3 mV. Based on the Butler-Volmer kinetics, Eq. (15), the local interfacial current density is estimated and shown in Fig. 8c. The current density also shows small variation within the electrode's solid phase. Fig. 8 shows an inhomogeneous distribution of lithium, and almost homogeneous distribution of voltage and interfacial current density during discharge at c-rate=1.

Structural heterogeneity is known to have greater influence physical and electrochemical processes when discharged at higher rates [31,46]. In order to further investigate the electrode heterogeneity, a discharge process at c-rate=5 was simulated. The lithium concentration, solid phase voltage, and interfacial current density results at c-rate=5 are shown in Fig. 9. It is clearly seen that higher discharge rate leads to higher lithium mass transport flux which results in larger lithium concentration inside the RVE (see Fig. 9a). As expected, the simulation results show higher inhomogeneity inside the electrode structure at c-rate=5 compared to c-rate=1. The electrode heterogeneity is more clearly observed by comparing the range of lithium concentration resulting from high and low rates (5 and 1 C, respectively) as shown in Table 7. The range of lithium concentration is significantly larger at 5 C than at 1 C. In addition, local solid phase voltage and interfacial current density are shown in Figs. 9b, and 9c, respectively, which are also greatly

influenced at higher rates. At c-rate=5, the voltage range reaches up to 12 mV, which is 4 times higher than 3 mV obtained at c-rate=1. The interfacial current density also distributes over a wider range at c-rates=5 compared to c-rate=1. The maximum range becomes approximately 8 A / m^2 at c-rate=5 which is higher than 2.8 A / m^2 achieved at c-rate=1. The histograms showing the electrode's physical and electrochemical properties at various SOCs at c-rate=5 are presented in Fig. 10. The distribution of the properties does not follow any particular trend. The macro-homogeneous models typically assume uniform distribution of the current density on the active material particles, however, in a realistic electrode, the current density distributes over a range due to heterogeneities.

Table 7. Lithium concentrations obtained at different SOCs of galvanostatically discharged electrode at 1 and 5 C (unit: mol / m^3)

C-rate	SOC=0.95	SOC=0.50	End of discharge
1	2282	12552	4536
5	19000	18400	16600

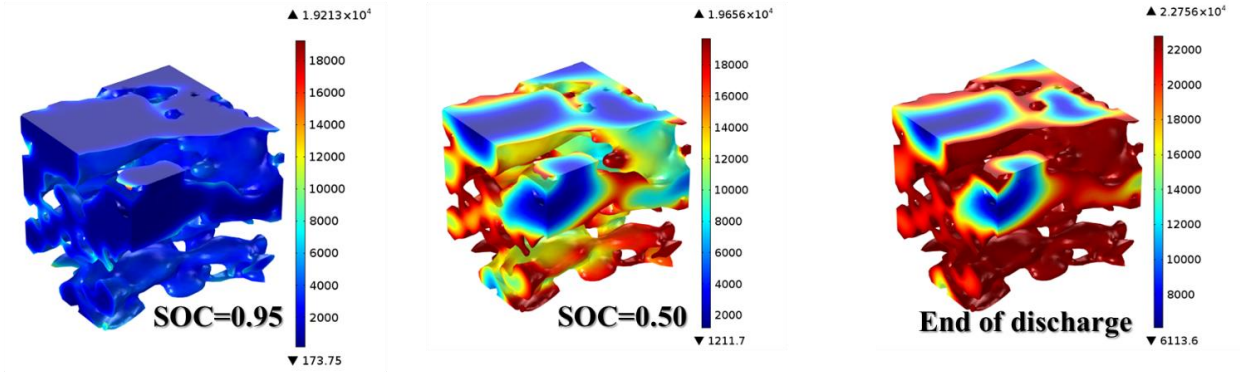

(a) Lithium concentration (mol / m^3)

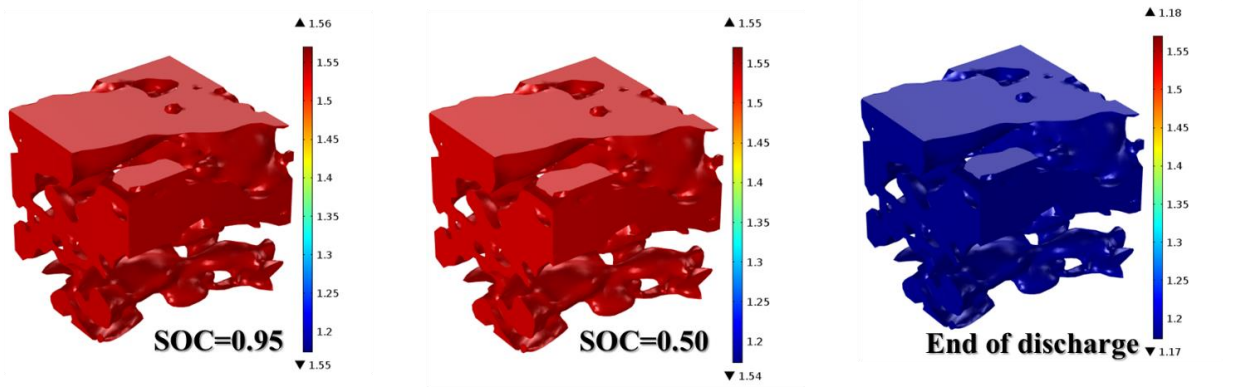

(b) Voltage (V)

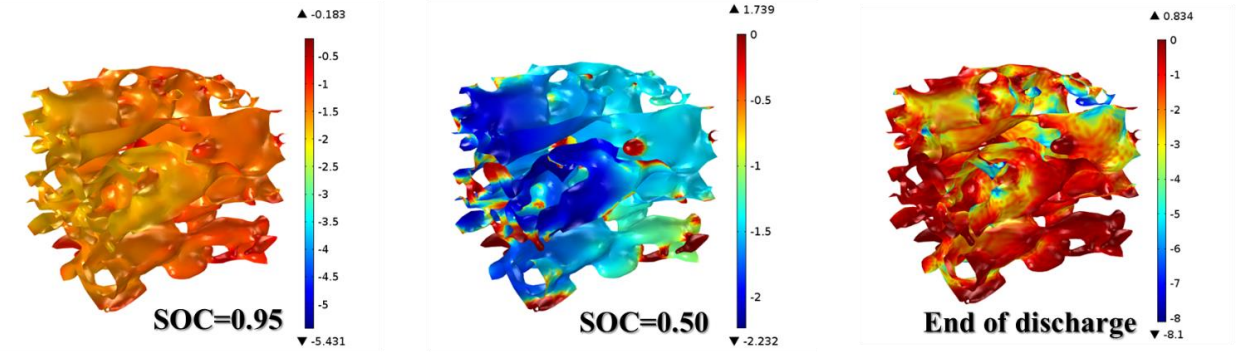

(c) Interfacial current density (A / m^2)

Figure 9. Distribution of physical and electrochemical properties in the RVE shown in Fig. 3 at various SOCs during galvanastatic discharge at 5 C.

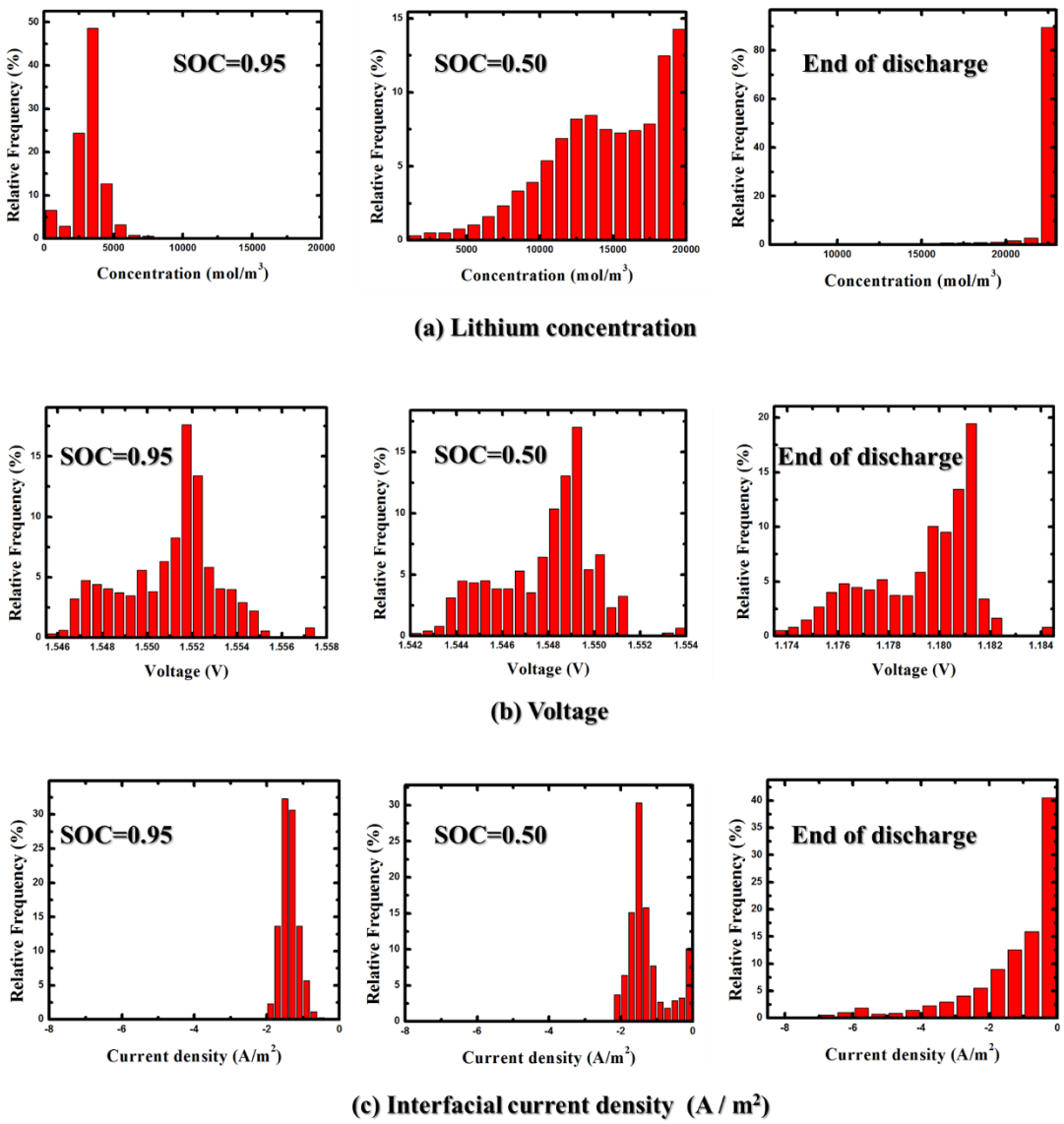

Figure 10. Histograms representing the distribution of physical and electrochemical properties in the RVE shown in Fig. 3 at various SOCs during galvanostatic discharge at 5 C.

5. Conclusions

The first 3D microstructural study of the LTO electrode based on multiple imaging mode synchrotron nano XCT was accomplished. The synchrotron with a 58 nm resolution was used to reconstruct 3D microstructure of the electrode, which was then characterized for its geometrical and electrochemical properties. The imaging was conducted using two different modes, absorption

contrast and Zernike phase contrast, to resolve the electrode's active material, CBD, and pore phases in different ways. The 3D image has revealed that some primary LTO nano-particles tend to agglomerate and form secondary micro-sized particles. Four secondary particles have been selected and their size, volume specific surface area, and degree of non-sphericity have been quantified for simulation. The secondary particles have shown different volume specific surface area ranging from 3.14 to 3.62 (μm^{-1}) and various degrees of sphericity from 0.71 to 0.91. The electrode's resistance to charge and mass transport have been quantified by estimating solid and pore domain tortuosities using two methods: 1) simulation based on mass transport analogy, and 2) pure geometry. The resulting tortuosities have shown that the commonly used Bruggeman relation for macro-homogeneous models is a poor estimator of the electrode tortuosity. Specifically, the pore domain in-plane and through-plane tortuosities have been estimated as 1.46, 1.69, and 2.07 which are higher than the Bruggeman tortuosity of 1.32. In addition, tortuosities obtained from both methods vary significantly depending on the direction, confirming highly anisotropic and heterogeneous nature of pore and solid domains. To further investigate the microstructural heterogeneity, a computational framework has been developed to simulate electrochemical performance of the LTO electrode. Unlike commonly used absorption contrast 3D structure, the current model took advantage of Zernike phase contrast reconstructed geometry. The lack of CBD in absorption contrast results in isolated active material particles, whereas Zernike phase contrast provides an integrated percolated network of active material and CBD together, making it suitable for FEM simulation. The model was an improvement over our previous RVE model as it now includes electron transport in the governing equations as well as lithium diffusion within solid. The model has been validated with the experimental data obtained from a coin half-cell. The simulation results have revealed irregular and non-uniform distribution of physical and electrochemical properties within the solid domain, which would not have been possible to predict using a macro-homogeneous model. This phenomenon is

attributed to the electrode's structural heterogeneity, which causes non-homogeneous mass and charge transport within the electrode structure. Structural heterogeneities have led to a wider distribution of properties at higher rates. Notably, the range of lithium concentration within the solid domain at the end of discharge reached 16,600 mol m^{-3} at C-rate=5, which is significantly higher than that of 4,536 mol m^{-3} at C-rate=1.

Acknowledgments

The present study was financially supported by the University of Akron, the Natural Sciences and Engineering Research Council of Canada (NSERC) through grants to Z.C. and the University of Waterloo. Also, this research funded to use resources of the Advanced Photon Source, a U.S. Department of Energy (DOE) Office of Science User Facility operated for the DOE Office of Science by Argonne National Laboratory under Contract No. DE-AC02-06CH11357.

Nomenclature

a	specific interfacial area (m^2/ m^3)
c	concentration of electrolyte (mol/m^3)
D	diffusion coefficient (m^2/s)
F	Faraday's constant, 96487 (C/mol)
i	current density (A/m^2)
I	total applied current density to the cell (A/m^2)
j_n	pore-solid flux of lithium ions ($mol/(m^3 .s)$)
k_0	reaction rate constant $(\text{mol m}^{-2}\text{s}^{-1}(\text{mol m}^{-3})^{-1.5})$
l	thickness (m)

R	universal gas constant (J/(mol. K))
t	time (s)
T	temperature (K)
t_+	transference number of lithium-ion with respect to the solvent
U	Open circuit potential of LTO (V)
x	spatial coordinate along the thickness of the cell

Greek letters

α	apparent transfer coefficient (kinetic parameter)
ε	porosity
σ	conductivity of solid domain (S/m)
ϕ	electric potential (V)
τ	electrode tortuosity

Subscripts

1	Solid phase
2	electrolyte phase
a	anodic
c	cathodic
eff	effective
ini	initial
LTO	$Li_4Ti_5O_{12}$
max	maximum
s	solid/electrolyte interface

References

1. G. E. Blomgren, *J. Electrochem. Soc.*, **164**, A5019–A5025 (2017) http://jes.ecsdl.org/lookup/doi/10.1149/2.0251701jes.

2. Y. H. Chen, C. W. Wang, X. Zhang, and A. M. Sastry, *J. Power Sources*, **195**, 2851–2862 (2010).

3. K. Feng et al., *Nano Energy*, **19**, 187–197 (2016) http://dx.doi.org/10.1016/j.nanoen.2015.10.025.

4. M. Biton, V. Yufit, F. Tariq, M. Kishimoto, and N. Brandon, *J. Electrochem. Soc.*, **164**, 6032–6038 (2017).

5. R. Mukherjee, R. Krishnan, T. M. Lu, and N. Koratkar, *Nano Energy*, **1**, 518–533 (2012) http://dx.doi.org/10.1016/j.nanoen.2012.04.001.

6. S. J. Harris, A. Timmons, D. R. Baker, and C. Monroe, *Chem. Phys. Lett.*, **485**, 265–274 (2010) http://dx.doi.org/10.1016/j.cplett.2009.12.033.

7. T. Hutzenlaub et al., *Electrochem. commun.*, **27**, 77–80 (2013) http://dx.doi.org/10.1016/j.elecom.2012.11.006.

8. M. Ender, J. Joos, T. Carraro, and E. Ivers-Tiffée, *Electrochem. commun.*, **13**, 166–168 (2011) http://dx.doi.org/10.1016/j.elecom.2010.12.004.

9. H. Mendoza, S. A. Roberts, V. E. Brunini, and A. M. Grillet, *Electrochim. Acta*, **190**, 1–15 (2016) http://dx.doi.org/10.1016/j.electacta.2015.12.224.

10. M. Ebner, D. W. Chung, R. E. García, and V. Wood, *Adv. Energy Mater.*, **4**, 1–6 (2014).

11. D.-W. D.-W. D.-W. D.-W. D.-W. Chung et al., *J. Electrochem. Soc.*, **161**, A422–A430 (2014) http://jes.ecsdl.org/cgi/doi/10.1149/2.097403jes.

12. J. M. Paz-Garcia et al., *J. Power Sources*, **320**, 196–203 (2016)

http://dx.doi.org/10.1016/j.jpowsour.2016.04.076.

13. D. S. Eastwood et al., *Nucl. Instruments Methods Phys. Res. Sect. B Beam Interact. with Mater. Atoms*, **324**, 118–123 (2014) http://dx.doi.org/10.1016/j.nimb.2013.08.066.

14. L. Wu, X. Xiao, Y. Wen, and J. Zhang, *J. Power Sources*, **336**, 8–18 (2016) http://www.sciencedirect.com/science/article/pii/S0378775316314458.

15. D. E. Stephenson et al., *J. Electrochem. Soc.*, **158**, A781 (2011) http://jes.ecsdl.org/cgi/doi/10.1149/1.3579996.

16. S. Komini Babu, A. I. Mohamed, J. F. Whitacre, and S. Litster, *J. Power Sources*, **283**, 314–319 (2015) http://dx.doi.org/10.1016/j.jpowsour.2015.02.086.

17. S. Frisco, A. Kumar, J. F. Whitacre, and S. Litster, *J. Electrochem. Soc.*, **163**, A2636–A2640 (2016) http://jes.ecsdl.org/lookup/doi/10.1149/2.0681613jes.

18. A. G. Kashkooli et al., *Electrochim. Acta*, **196**, 33–40 (2016) http://www.sciencedirect.com/science/article/pii/S0013468616304248.

19. M. Doyle and J. Newman, *Electrochim. Acta*, **40**, 2191–2196 (1995).

20. H. Zarrin et al., *Electrochim. Acta*, **125**, 117–123 (2014) http://dx.doi.org/10.1016/j.electacta.2014.01.022.

21. D. A. G. Bruggeman, *Ann. Phys.*, **416**, 636–664 (1935) http://doi.wiley.com/10.1002/andp.19354160705.

22. B. Tjaden, S. J. Cooper, D. J. Brett, D. Kramer, and P. R. Shearing, *Curr. Opin. Chem. Eng.*, **12**, 44–51 (2016) http://dx.doi.org/10.1016/j.coche.2016.02.006.

23. I. V. Thorat et al., *J. Power Sources*, **188**, 592–600 (2009).

24. S. J. J. Cooper et al., *J. Power Sources*, **247**, 1033–1039 (2014) http://dx.doi.org/10.1016/j.jpowsour.2013.04.156.

25. A. G. Kashkooli et al., *J. Power Sources*, **307**, 496–509 (2016) http://linkinghub.elsevier.com/retrieve/pii/S0378775315307461.

26. D. Kehrwald, P. P. R. Shearing, N. P. N. Brandon, P. K. P. Sinha, and S. S. J. S. Harris, *J. Electrochem. Soc.*, **158**, A1393–A1399 (2011) http://jes.ecsdl.org/cgi/doi/10.1149/2.079112jes.

27. B. Yan, C. Lim, Z. Song, and L. Zhu, *Electrochim. Acta*, **185**, 125–141 (2015) http://linkinghub.elsevier.com/retrieve/pii/S0013468615306678.

28. A. G. Kashkooli et al., *J. Appl. Electrochem.*, **47**, 281–293 (2017) http://link.springer.com/10.1007/s10800-016-1037-y.

29. J. Li, Z. Tang, and Z. Zhang, *Electrochem. commun.*, **7**, 894–899 (2005).

30. D. Ahn and X. Xiao, *Electrochem. commun.*, **13**, 796–799 (2011) http://dx.doi.org/10.1016/j.elecom.2011.05.005.

31. B. Yan, C. Lim, L. Yin, and L. Zhu, *J. Electrochem. Soc.*, **159**, A1604–A1614 (2012) http://jes.ecsdl.org/cgi/doi/10.1149/2.024210jes.

32. L. Cheng et al., *J. Mater. Chem.*, **20**, 595–602 (2010) http://xlink.rsc.org/?DOI=B914604K.

33. V. De Andrade et al., *SPIE Newsroom*, 2–4 (2016) http://www.spie.org/x118318.xml.

34. D. Gürsoy, F. De Carlo, X. Xiao, and C. Jacobsen, *J. Synchrotron Radiat.*, **21**, 1188–1193 (2014) http://scripts.iucr.org/cgi-bin/paper?S1600577514013939.

35. D. M. Pelt and K. J. Batenburg, in *Proceedings of the 2015 International Meeting on Fully Three-Dimensional Image Reconstruction in Radiology and Nuclear Medicine.*, (2015).

36. C. Lim et al., *J. Power Sources*, **328**, 46–55 (2016) http://dx.doi.org/10.1016/j.jpowsour.2016.07.119.

37. M. Doyle, *J. Electrochem. Soc.*, **143**, 1890 (1996).

38. M. Guo, G. Sikha, and R. E. White, *J. Electrochem. Soc.*, **158**, A122 (2011).

39. G. Ning and B. N. Popov, *J. Electrochem. Soc.*, **151**, A1584 (2004) http://jes.ecsdl.org/cgi/doi/10.1149/1.1787631.

40. S. Stewart et al., *J. Electrochem. Soc.*, **155**, A253 (2008).

41. J. Christensen, V. Srinivasan, and J. Newman, *J. Electrochem. Soc.*, **153**, A560 (2006).

42. J. Newman and W. Tiedemann, *AIChE J.*, **21**, 25–41 (1975) http://doi.wiley.com/10.1002/aic.690210103.

43. C. Lim, B. Yan, L. Yin, and L. Zhu, *Electrochim. Acta*, **75**, 279–287 (2012).

44. A. Ghorbani Kashkooli et al., *Electrochim. Acta*, **247**, 1103–1116 (2017) http://linkinghub.elsevier.com/retrieve/pii/S0013468617315074.

45. V. Srinivasan and J. Newman, *J. Electrochem. Soc.*, **151**, A1517 (2004).

46. M. Smith, R. E. García, and Q. C. Horn, *J. Electrochem. Soc.*, **156**, A896 (2009) http://jes.ecsdl.org/cgi/doi/10.1149/1.3216000.